Ceramics International 45 (2019) 3627–3633

Contents lists available at ScienceDirect

Ceramics International

journal homepage: www.elsevier.com/locate/ceramint

Vacuum sintered lunar regolith simulant: Pore-forming and thermal conductivity

Lei Song[a,c], Jiao Xu[a,*], Shuqian Fan[a], Hong Tang[b], Xiongyao Li[b], Jianzhong Liu[b], Xuanming Duan[a,*]

[a] Chongqing Key Laboratory of Additive Manufacturing Technology and System, Chongqing Institute of Green and Intelligent Technology, Chinese Academy of Sciences, No. 266 Fangzheng Avenue, Beibei District, Chongqing 400714, PR China
[b] Center for Lunar & Planetary Sciences, Institute of Geochemistry, Chinese Academy of Sciences, 99 Lincheng West Road, Guiyang 550081, PR China
[c] University of Chinese Academy of Sciences, Yanqihu Campus, Huaibei Town, Huaibei Zhuang, Huairou District, Beijing 101407, PR China

ARTICLE INFO

Keywords:
Lunar regolith simulant
Sintering
Thermal conductivity
Porosity
Silicate

ABSTRACT

Lunar regolith molding technologies are receiving an increasing attention in lunar exploration program. Most studies are carried out in the air on earth, ignored the effects of high vacuum (~ 10^{-12} mbar) on the lunar surface. This paper presents the results of a study aimed at assessing the effect of vacuum on the sintering of low Ti basalt type lunar simulant CLRS-1. The results show that porous sample with density of 1.19 g cm^{-3} can be obtained by sintering at 1100 °C under vacuum, which has much lower thermal conductivity (0.265 W m^{-1} K^{-1}) than concrete and other lunar resource derived structural materials. It could potentially be applied as the thermal insulation material for the Moon base construction. The pore-forming mechanism in vacuum was investigated. It was found that evaporation of the products of solid dissolved mineral crystals led to a great deal of weight loss and inhibited the densification during sintering.

1. Introduction

As a celestial body nearest to Earth, the Moon has been desired to be utilized as a transit station not only for exploration of Mars or farther galaxies, but also for developing the rich minerals and energy resources based on the currently sustainable development requirements of human society [1]. To realize the human colonization on the Moon, an imperative lunar base for sustainable long-term human presence must be established at first. However, it is too expensive to transport building materials from Earth; for example, it could cost up to $2 million to transport an ordinary brick to the Moon [2]. Thus, the in-situ resource utilization (ISRU) of construction materials becomes the natural and best choice [3,4]. The dry and powdery lunar regolith with 30 μm to 1 mm and irregular shapes derived from fragmentation of the rocks and meteorolite is everywhere on the Moon surface, which is the most economical and feasible construction materials to build lunar bases.

The properties of lunar regolith have been intensely investigated, and various lunar regolith simulants such as JSC-1, EAC-1, DNA-1, FJS-1, OB-1 and CLRS-1 have been developed by America, Europe, Japan, Australia and China [5–7]. These simulants are effective replica of lunar regolith from Apollo missions, in which main components are volcanic vitreous, plagioclase, pyroxene, olivine and magnetite. The sintering of simulated lunar regolith has attracted wide attention. There are many researches on the sintering methods of lunar regolith simulants, including furnace sintering [8], microwave sintering [9–11], laser sintering [12–17] and solar sintering [6,18,19]. However, lunar regolith is a complex multicomponent inorganic nonmetallic material. The molding process may be drastically complicated. Hence, sintering process and sintering properties for lunar regolith should be discussed more deeply to improve their molding technology.

It should be noted that the atmospheric pressure on Moon is about 3×10^{-12} mbar compared to about 1 bar on Earth, which indicates that the vacuum sintering properties of lunar regolith simulants have to be discussed. Normally, under vacuum condition, the wettability of liquid phase, oxygen partial pressure and melting point of components will be different from that in air [20]. Thus, the vacuum atmosphere generally leads to the reduction in the inner pores of the samples during sintering. More than that, many researches have indicated that vacuum sintering could improve the densification to prepare transparent ceramics [21–23]. Although the vacuum sintering of lunar regolith simulants should more closely simulate sintering condition on the Moon, few reports have been found [24]. More works for vacuum sintering properties of lunar regolith should be carried out for the lunar base construction preparation and scheme design. It is quite possible to obtain

* Corresponding authors.
E-mail addresses: xujiao@cigit.ac.cn (J. Xu), xmduan@cigit.ac.cn (X. Duan).

https://doi.org/10.1016/j.ceramint.2018.11.023
Received 27 August 2018; Received in revised form 1 November 2018; Accepted 5 November 2018
Available online 06 November 2018

the information for main physicochemical variations and major influence of components for sintering.

In this paper, we investigated the vacuum sintering process of a lunar regolith simulant, CLRS-1, as well as physicochemical properties such as density, thermal conductivity performance and composition evolution of the sintering samples for the first time. In addition, when the sintering temperature was lower than a certain value, the sintered samples densified with the increase of sintering temperature, but when the sintering temperature was higher, the unusual pore formation occurred. Thus the pore-forming mechanism of sintered samples was further explored.

2. Materials and methods

2.1. Materials

The lunar regolith simulant used in this research was the Chinese national standard sample low-titanium lunar simulant CLRS-1 (GSB 01-2186-2008) supplied by Institute of Geochemistry, Chinese Academy of Sciences. The simulated lunar regolith with a relatively wide particle size was obtained by grinding and crushing form volcanic ash. The Si, Al, Fe, Mg and Ca are the main elements of CLRS-1 as shown in Table 1S, which is derived from volcanic vitreous, plagioclase, pyroxene, olivine and magnetite [25]. The composition of CLRS-1 is very similar to the actual lunar regolith sample collected from the lunar surface retrieved by the Apollo mission.

The CLRS-1 powder as shown in Fig. 1S was sieved using a sieve with the apertures of 200 mesh and maintained an sharp and irregular shape. The powder was then dried in an oven at 110 °C for 24 h. The dried powder of 0.6 g placed in a cylindrical stainless steel mold with the inner diameter of 20 mm was compressed under 24 MPa pressure, and then kept this pressure for 4 min to form a thin disc with a thickness of about 1 mm.

2.2. Sintering experiments

A commercial tube type vacuum sintering furnace (BTF-1200C, BEQ, China) with Edwards vacuum pump (RV8) was employed for vacuum sintering. The prepared CLRS-1 thin disc samples were put on an Al_2O_3 substrate placed in a quartz boat for sintering. After the vacuum degree was reached to 2.0–5.0 × 10^{-3} mbar, the samples were heated with the heating rate of 15 °C min^{-1}, and held at the target temperature for 15 min. The target temperatures were set at 700, 800, 900, 1000, 1050, 1100 and 1150 °C, respectively. Meanwhile, the same sintering experiments in air were also performed to compare with vacuum sintering. After finishing the sintering, the furnace was opened for rapid natural cooling. The obtained CLRS-1 sintering samples were used for characterization.

2.3. Characterization

For carrying out the nondestructive examination of the CLRS-1 sintering samples, the micro-CT imaging equipment with a CT analyzer (CD-5BX/nCT, China) [26] contained a 60 kV/150 mA micronano-focus X-ray tube were performed. The morphology and elemental distribution were measured using a thermal field scanning electron microscope (SEM) (JSM-7800F, JEOL, Japan) and the attached energy-dispersive X-ray spectrometer (EDS). The crystalline phases presented in green body and sintered samples were identified by X-ray diffraction analysis (X'Pert3 Powder, Panalytical, Netherlands) using a Cu/Kα radiation run at 40 kV/40 mA. Laser Raman spectrometer (InVia-Reflex, Renishaw, England) with the laser wavelength of 532 nm was utilized for characterizing the Raman spectra of compounds in the CLRS-1 sintering samples. The X-Ray Fluorescence spectroscopy (XRF-1800, Shimadzu, Japan) based on General rules for analysis of JY/T016-1996 wavelength dispersive X-ray fluorescence spectrometry was used to determine elemental composition of samples.

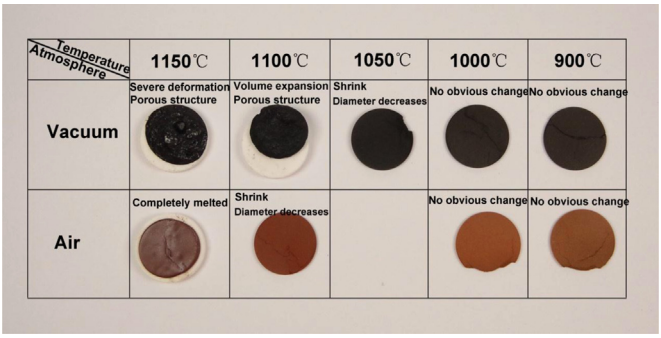

Fig. 1. Photos of samples sintered in air and vacuum at different temperatures.

The bulk densities of CLRS-1 sintered samples were measured applying the Archimedes method in a solid densitometer (BR-120, Beyond Test, China). Thermal conductivities of CLRS-1 sintered samples were measured by a laser thermal conductivity testing instrument (LFA 457, Netzsch. Ltd, German). For the thermal conductivity measurement, the samples were prepared as cylinders with the diameter of 12.7 mm and the thickness of 1–3 mm through grinds by sand papers prior. The conductive silver paste was used to stick the 12.7 mm × 0.8 mm sheet copper with high thermal conductivity on the top and bottom of circular surfaces for the porous samples due to the absorbed laser pulse energy can be quickly transferred.

3. Results and discussion

3.1. Porous structure and thermal conductivity

The appearances of the samples sintered in vacuum and air showed different color and shape variations. The colors of samples sintered in vacuum were deepened to dark gray with increasing the sintering temperature, while that of in air was similar to brick red (Fig. 1), which is quite different from the green body of CLRS-1 as shown in Fig. 2(a). Interestingly, the shrinkage and deformation of samples were distinctly observed at the sintering temperature of 1100 °C in vacuum, comparing to the samples sintered without variation in air. The diameter of the sintered disc sample in vacuum at 1100 °C shrunk from 20 mm to about 16 mm, its thickness increased from 1 mm to about 5 mm (Fig. 2(b)) and the shape became non-uniform compared to the green body. When the sintering temperature was increased to 1150 °C, the abundant molten phenomena of the samples were observed, in which the molten phase sprawled to the edge of Al_2O_3 substrate (Fig. 2(c)) compared to the samples sintered at 1100 °C. However, these phenomena have not been found from the samples sintered in air, although a weak molten phenomenon was observed. The extrinsic morphology feature of the samples indicated the possibility of macro pores formed inside the sample sintered in vacuum.

The micro-CT imaging technique was performed to reveal the inner pore morphology of sample sintered in vacuum at 1100 °C. The obtained micro-CT 3D images can identify that many pores with various sizes and shapes are inside the sintered sample (Fig. 2(b)) as shown in Fig. 2(d). The 2D sliced images from the A-A position and the contacted Al_2O_3 substrate (Fig. 2(e) and (f), respectively) clearly show that a macro pore with large size and irregular shape is formed at the sample center, meanwhile the smaller pores with spherical shape are also generated. These features are also presented in the sample sintered in vacuum at 1150 °C (Fig. 2(c)) as shown in Fig. 2S(a) and (b). However, no macro pores is observed in sample sintered in vacuum at 1050 °C and the micro-CT images exhibit a dense structure inside the sample (Fig. 2S (c)), which means the formation of macro pores started above 1050 °C. The obtained porous sample of lunar regolith simulant sintered in vacuum could be expected to possess interesting properties.

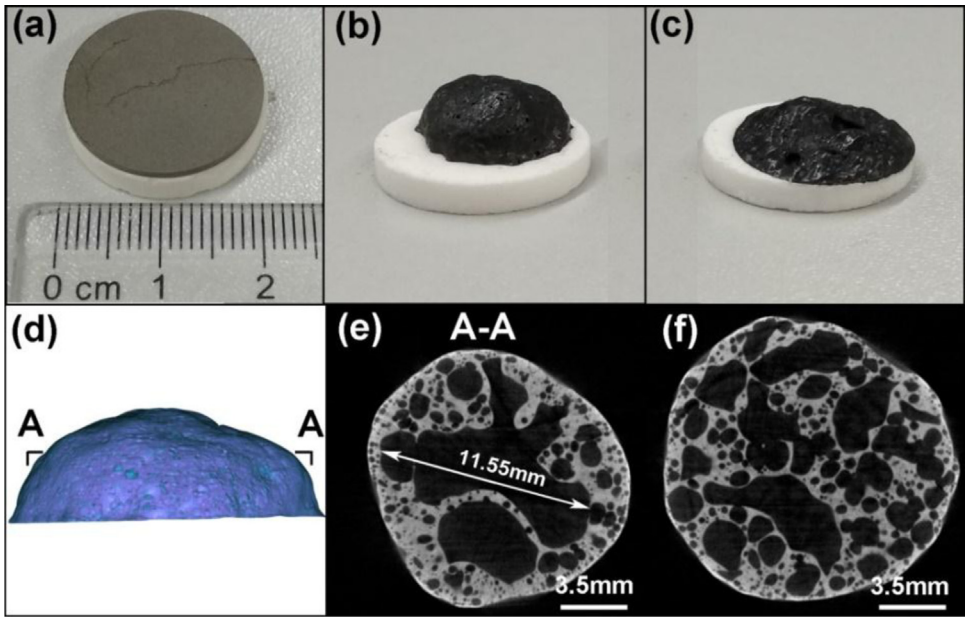

Fig. 2. (a) The photos of green body, (b) sample sintered in vacuum at 1100 °C and (c) 1150 °C; (d) micro-CT 3D imaging of sample in (b); (e) micro-CT 2D slices from the middle and (f) bottom that contact with Al_2O_3 substrate for the sample sintered in vacuum at 1100 °C by micro-CT. "A-A" represents a slice that looks down from top to bottom.

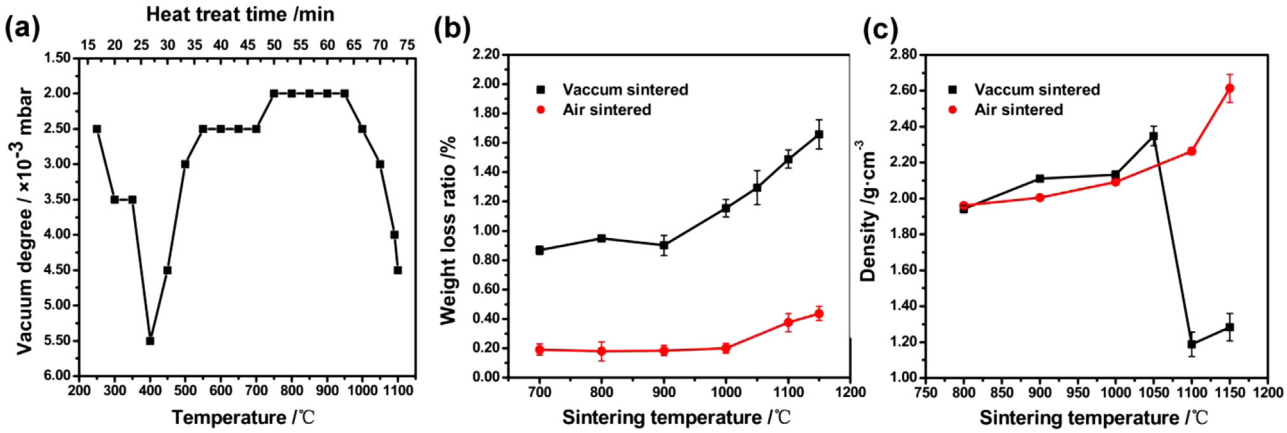

Fig. 3. (a) The variation of vacuum degree in the sintering process for porous sample sintered at 1100 °C in vacuum. (b) The weight loss ratio and (c) the density for all samples sintered in air and vacuum under different sintering temperature.

To clarify the effect of temperature on sintering process, the vacuum degree variation in sintering chamber with time and temperature history in heat treatment process (Fig. 3(a)) and sintering temperature trends to weight loss ratio (Fig. 3(b)) had been measured and plotted. When temperature was raised to 400 °C, the vacuum degree declined significantly, which may be caused by the volatilization of a second type of water that presumably bound in lattices of secondary minerals along with other volatile oxides substances [27]. Then the vacuum degree ascended and was kept between 2.0 and 2.5 × 10^{-3} mbar until 950 °C. Continue to heat up, the vacuum degree declined again and kept declining to 4.5 × 10^{-3} mbar at 1100 °C. After holding at 1100 °C for 15 min, the vacuum degree finally declined to 6.5 × 10^{-3} mbar. The vacuum degree variation in sintering chamber is mainly affected by the evaporation and diffusion of substances at high temperature. Therefore, vacuum degree variation is closely related to mass loss and what can be predicted is that the loss of material was quite small between 550–950 °C and considerable loss of material started from 950 °C, which is consistent with the observation from Fig. 3(b). However, no macro pores were observed in samples sintered below 1100 °C, which may be due to that the evaporation rate of the substances was slower than the mass transfer rate. When sintering temperature rose up to 1100 °C, the evaporation rate of the substances was faster which hindering the formation and contraction of closed pores [28]. Furthermore, the content of liquid phase increases with sintering temperature, which leads to the increase of mass transfer rate, and part of pores shrunk, thus the density of sample sintered in vacuum at 1150 °C increased.

The pores would inevitably affect the density of materials. Thus, the densities of samples sintered under different conditions have been measured and plotted in Fig. 3(c). The result shows that porous samples sintered in vacuum at 1100 °C has the lowest density 1.19 g cm^{-3}, which is nearly half of that at 1050 °C (2.35 g cm^{-3}) and much lower than density of air sintered samples (2.26 g cm^{-3}) at the 1100 °C. The density of samples sintered in vacuum at 1150 °C increases due to melting of components. Different from the samples sintered in vacuum, the density of samples sintered in air increases with sintering temperature. Besides, vacuum sintered samples have higher density than air sintered samples below 1050 °C. These phenomena are consistent with the powder sintering theory [29] as illustrated below. Generally, in the sintering process, there are a large number of pores include primordial pores and that of formed by particle rearrangement. Then, the pores gradually shrink and deform due to the mass transfer between particles, and finally form isolated closed pores. During this process, the density of samples will gradually increase with sintering temperature. The appearance of liquid phase in sintering process is beneficial to further densification of samples. Vacuum atmosphere could promote wettability of liquid phase and the removal of gas to transform the open

pores into closed pores [30,31], so vacuum sintered samples usually have higher density. However, the mass transfer of the complex multiphase simulated lunar regolith system during sintering process in our experimental will be more complicate. The process of porosity reduction will be hindered when substances evaporate in large quantities and the closed pores will have the tendency to swell under vacuum due to the pressure difference, which explains the reason for the low density of samples sintered at 1100 °C under vacuum. This phenomenon is different from the densification process in general sintering.

Besides, Fig. 3(b) shows that the weight loss ratio in vacuum sintering is about four times that in air sintering. As we know, the vacuum degree on the Moon is much higher than our experiments. Obviously, the vacuum condition has a very great influence on the lunar regolith simulants sintering properties. The unexpected macro-pore formation, the weight loss and the density decrease of samples in our experiment for only $\sim 10^{-1}$ Pa vacuum sintering condition demonstrate the significance of vacuum sintering research for lunar regolith. Thus, the major influence of different components in samples should be figure out and further analyses are needed to confirm which components evaporated during sintering. And the pore-forming mechanism should be clarified.

Porous materials usually have good thermal insulation properties. Hence, thermal conductivities of porous samples and dense samples at room temperature 25 °C, daytime temperature of the Moon 123 °C [32] and a possible heat treatment temperature 600 °C are measured and listed in Table 1. The thermal conductivity at room temperature of porous sample sintered in vacuum at 1100 °C is only 0.265 W m^{-1} K^{-1}, and that of the densest sample (sintered at 1050 °C) is 0.900 W m^{-1} K^{-1} and about 3.4 times to porous sample. The values for porous sample are lower than those of some light concretes [33] and dense concretes [34], and also lower than that of glasses (2.0 ± 0.3 W m^{-1} K^{-1}) prepared from simulated compositions of lunar regolith simulant JSC-1A by Pinheiro et al. [35] Moreover, the thermal conductivity of samples shows the characteristics of increasing with temperature and density except sample sintered in vacuum at 1000 °C. It is known that, in air condition, there are three primary heat transfer mechanisms including heat conduction, convection and thermal radiation. Considering that convection and thermal radiation only happen inner the pores of materials, so these two modes of heat transfer in dense materials can be ignored on the basis of the size of pores is quite small. However, for porous materials, convection and thermal radiation could not be ignored, especially the radiation heat transfer flow which is proportional to the fourth power of the temperature [36], and that means the higher the temperature, the more heat the radiation is. This is consistent with the results in the Table 1. At 600 °C, the thermal conductivity of porous sample increases significantly to 1.326 W m^{-1} K^{-1}, while that of dense samples is not significantly changed.

The results show that lightweight porous samples have low thermal conductivity at room temperature and lunar surface temperature, which may lead to a good application prospect to buildings with extreme temperature conditions on the Moon; for example, it can be used as the thermal insulation layer for the lunar bases. Actually, similar lightweight foam cement has already been used as thermal insulation board on earth [37]. However, the temperature difference on the surface of Moon is much larger than that on the earth, which puts forward higher requirements for energy conservation, so more thermal insulation materials are needed on Moon. In addition, the thermal conductivities of porous samples in high temperature sintering are relatively good, which provides the possibility for more applications. The last remarkable thing is that there are only two modes of heat transfer, namely heat conduction and thermal radiation [38], in vacuum. Therefore, the thermal conductivity values obtained in our experiment is quite possibly higher than that of sample tested on the Moon, because of the inhibitory effect of large pores on thermal conductivity and thermal radiation. This means the heat insulation property may be even better on the Moon for our sample.

Table 1
The thermal conductivity and specific heat of air sintered samples and vacuum sintered samples at 25 °C, 123 °C and 600 °C. To make sure the shape preservation of tested sample, the sample sintered at 1050 °C and 1100 °C are chosen.

Sintering atmosphere	Sintering temperature/°C	Density/ g cm^{-3}	Test temperature/ °C	Thermal conductivity/ W m^{-1} K^{-1}
Vacuum	1100	1.126	25	0.265
			123	0.359
			600	1.326
	1050	2.346	25	0.900
			123	1.039
			600	1.126
Air	1100	2.342	25	0.769
			123	0.897
			600	0.960

3.2. Evaporated substances and pore-forming mechanism

3.2.1. The XRD analysis

Phase evolution, morphology and composition change during sintering process were investigated to discover the evaporated substances. The XRD patterns for green body and vacuum sintered samples in Fig. 4 indicate that the crystalline phases of all samples are mainly composed of plagioclase (Ca,Na)[(Al,Si)$_4$O$_8$] (PDF#99–0012 and PDF#99–0001) forsterite Mg_2SiO_4 (PDF#99–0052), magnetite Fe_3O_4 (PDF#99–0073) and diopside $CaMgSi_2O_6$ (PDF#99–0045) phase, and the main difference among samples is the peak strength. There are broad amorphous scattering in green body and samples sintered in vacuum at 800 °C and 900 °C respectively. Then the broad amorphous scattering disappeared at higher sintering temperature which may be related to enhanced crystallization [27]. Besides, as is known, the amorphous phases usually have low softened temperature [39,40], for instance, that lower than 700 °C for silicate glass [41] and lower than 900 °C for aluminosilicate glass [42,43]. While silicate and aluminosilicate mineral crystals in lunar regolith system usually have a melting point of higher than

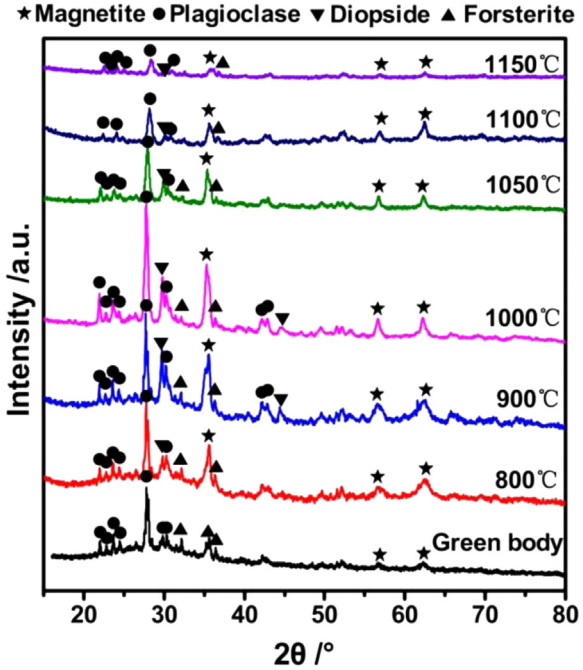

Fig. 4. The comparisons of XRD patterns of green body with samples sintered in vacuum at different temperatures.

1000 °C. Thermodynamically, softened amorphous phase would be more volatile than crystal phase under vacuum because of the instability of disordered structure of softening phase [44,45]. Therefore, non-ignorable weight loss happened in sintered samples at low sintering temperature (below 1000 °C) in Fig. 3(b) may mainly attribute to amorphous phase.

It is remarkable that the diffraction peaks are strengthen with increase of sintering temperature below 1050 °C, and then decrease. This may be due to the serious deformation and the formation of porous structure of the samples from 1050 °C. Especially, compare to the XRD peak of plagioclase phase at 30.248°, the relative peak intensity of diopside phase at 29.845° and 44.343° increases with the sintering temperature below 1000 °C, and then decreases above 1000 °C, which indicates that the amount of diopside crystal decrease or worse crystallinity above 1000 °C sintering temperature. Generally, this phenomenon may be related to solid dissolution of alkali oxides which came from molten amorphous phase in mineral crystals and then decrease the melting point of dissolving part [46]. However, unlike the reports [47], only the decrease of peak intensity has been observed instead of the broadening for peak width in our work, which confirms that solid dissolution with lower melting temperature has vaporized at higher temperature or under vacuum. Hence, the increase of the mass loss rate above 1000 °C in air may be caused by vaporization of amorphous and solid solution. Under vacuum, the melting and vaporization temperature of the material will normally decrease, thus the vaporization speed in vacuum is faster than that of in air at the same temperature. That is why the mass loss in vacuum is nearly four times higher than that of in air.

In addition, the XRD peaks of magnetite at 56.935° and 62.520° are very weak in green body, and become stronger after sintering. This is because of the continuously creation of Fe_3O_4 crystals. Differently, there is hematite phase independently observed in the XRD pattern of air sintered samples after 900 °C heat treatment without magnetite XRD signal (Fig. 3S). This explains the reddened process of air sintered samples shown in Fig. 1. Thus, the XRD patterns show that the vacuum sintering process has a great effect on the types of iron oxides in sintered samples by lack of O_2 in sintering [27].

Table 2
EDS data of atom composition (sample sintered in vacuum at 1100 °C) marked in Fig. 4.

Element	Atomic%					
	A	B	C	D	E	F
Na	1.10	1.47	3.87	4.09	0.96	2.04
Ca	0.81	1.39	3.03	2.75	0.80	8.60
Mg	2.61	2.47	0.86	0.70	0.54	0.89
Al	3.11	3.13	8.74	9.20	1.87	5.21
Si	5.20	5.85	17.96	17.27	3.43	9.01
K	0.61	5.41	1.80	1.00	0.33	1.26
Fe	29.93	23.62	3.72	1.31	74.15	16.66
Ti	5.00	4.44	1.33	0.34	3.51	0.00
O	51.63	52.23	58.67	63.33	14.41	56.33
Total	100	100	100	100	100	100

3.2.2. The SEM and EDS analysis

Fig. 5 shows the characteristic SEM zones of the porous sample sintered in vacuum at 1100 °C. Fig. 5(a) and (b) are respectively the SEM images of cross section and surface of sample, which indicate that a large number of open and close pores with size of 20–200 μm existing both on the surface and inside of the sample, and the smallest pore size may reach nanometer level according to the magnified images. The magnified image Fig. 5(c) shows that the crystal morphologies of different regions are very different and the magnified images of feature areas I, II and III are shown in Fig. 5(d)-(f). According to Fig. 5(d) and Table 2, there is a mass of irregular lamellar crystal with very high content of Fe and Si, and higher content of Mg as point A than point C, D, E and F. While, Fig. 5(e) is mainly composed of tabular crystal as point C with high content of Al and Si and granular crystal as point B with content similar to point A. Combined with the results of XRD and

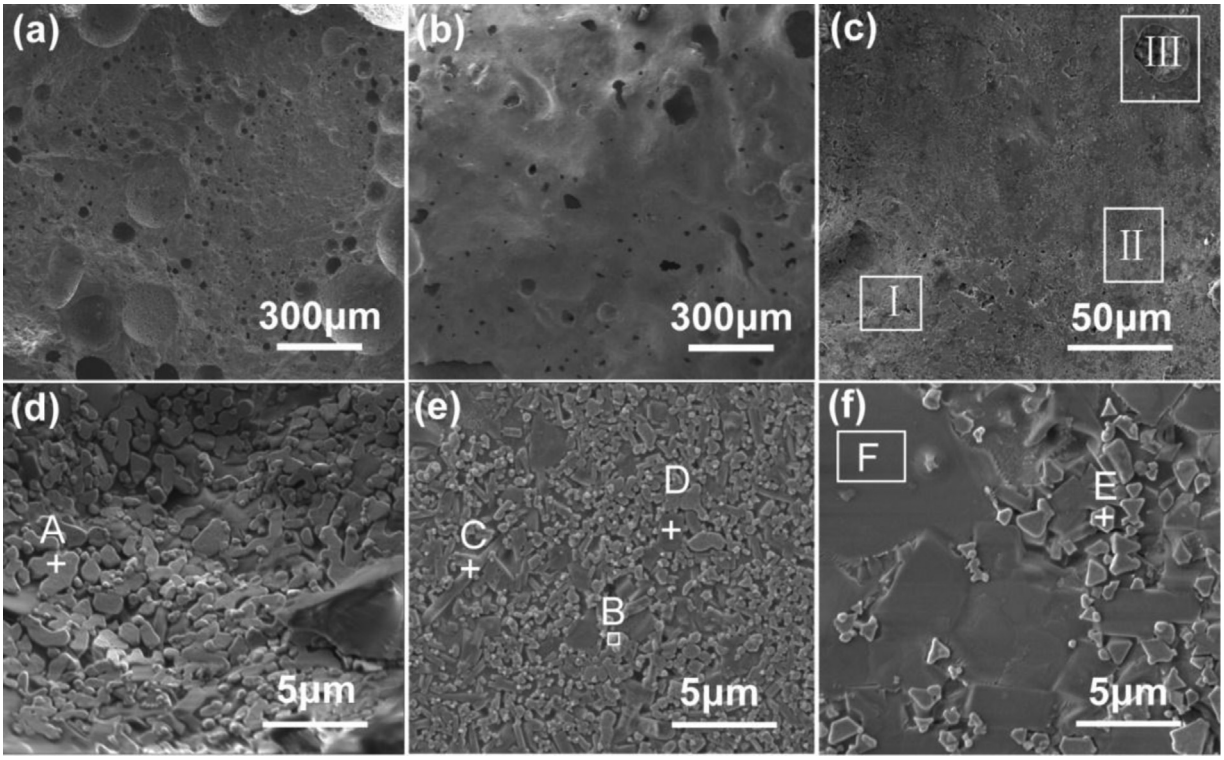

Fig. 5. SEM images of cross section (a), surface macrograph (b) (c), magnified images of feature areas (d) (e) and the pore micrograph (e) of sample sintered in vacuum at 1100 °C. Figure (d) is the magnified image of zone I, Figure (e) is the magnified image of zone II, and Figure (f) is the magnified image of zone III.

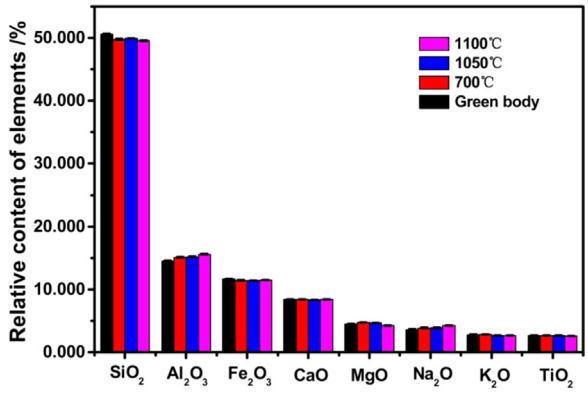

Fig. 6. Relative content of elements between samples sintered in vacuum at 700 °C, 1050 °C, 1100 °C and green body acquired via XRF.

EDS results, the grains at point A and B are probably mainly composed of the magnetite (Fe_3O_4) and forsterite (Mg_2SiO_4) phase. Furthermore, although the morphology of the crystal at point D is square, it has similar content with point C and the grains are mainly plagioclase ($(Ca,Na)[(Al,Si)_4O_8]$) phase. Moreover, abnormally large grains and triangular crystal can be found in the pore structure in amplified area III (Fig. 5(f)), namely the macroscopic pore region. The EDS data of point E indicates that the triangular phase is mainly iron oxide phase, which is also been observed in the study of Hintze et al. [6] However, the composition of the substance at smooth zone F in Fig. 5(f) is quite different from that of the others point. The content of Al and Si of zone F is similar to point A and B, despite lower Mg and higher Ca content. Thus we consider that the substance at zone F may be the product of the evaporation of Mg in Ca-Mg silicates such as diopside. Of course, the evaporation can lead to the generation of macro pores.

3.2.3. The XRF analysis and pore-forming mechanism

Further analyses were carried out to confirm what the evaporated substances exactly are. A comparison of the element concentrations by XRF test between sintered samples and green body is shown in Fig. 6. The concentrations of Si and Fe had decreased after sintering at 700 °C, while the relative content of Na, Mg and Al increased. As discussed in XRD results, in consideration of high molten point of mineral crystals, the first evaporated substances in samples below 700 °C could only be amorphous phase (or mineral glass) with Si and Fe elementals. Besides, in the system of silicate minerals, the Si-O and Al-O skeletons are mainly combined by the covalent bonds, while the excess negative charge is compensate for by other cations, in the form of ionic bonds [48]. Therefore, it is easy to understand that less loss of Al is owing to the extreme stability of the covalent bonds. Further comparison of the difference between samples sintered at 1050 °C (the dense sample) and 1100 °C (the porous sample) indicates that the concentrations of Si and Mg significantly decreased, which implies that the substances evaporated and resulted in the formation of the macro pores may contain a great quantity of Si and Mg, in accord with the observation from SEM (Fig. 5(f)). It is common believed that the melting point of magnesium containing minerals is extremely high, such as 1890 °C for pure forsterite and 1391 °C for pure diopside in our materials at standard atmospheric pressure. Nevertheless, there is one exception that enstatite has a quite low melting temperature, namely between 630 °C and 1000 °C. There is few report on the transformation of forsterite to enstatite by solid solution, but according to Chen et al. [49], enstatite is generated at 1100 °C in $MgO\text{-}SiO_2$ system. Hence, we speculate that low melting point solid solution such as enstatite was produced by diopside solid dissolve in the complex system, and then the solid solution evaporated under high temperature in vacuum.

Take into account variation of vacuum degree in sintering chamber during sintering, weight loss ratio of samples and results of XRF, the change of components of porous samples during sintering can be summarized as follow. From room temperature to ~ 400 °C, the main change of the sample is the evaporation of water, including the water molecules adsorbed on the surface of particles and in the crystal lattice. From ~ 400 °C to ~ 950 °C, the amorphous phase in sample melted and gradually evaporation, which results in the reduction of the elements contained in the amorphous phase, including Si, Al, Ca and Fe. From ~ 950 °C to ~ 1050 °C, the molten amorphous phase solid dissolved in mineral crystals, which leads to decrease of the melting point of solid dissolving part [46]. During this process, a small amount of Mg element evaporated and the peak intensity of diopside phase has decreased at the same time, which means the diopside phase was quite possibly solid dissolved and produced a solid solution such as enstatite with a lower melting point. However, the amount of solid solution is quite low. From ~ 1050 to 1100 °C, more and more solid solution with low melting point such as enstatite was generated and evaporated. The evaporation hindered the transfer of materials in sintering and thus the macro pores formed. It is surely that other elements may also be evaporated in this process, but their quantity is small enough to be negligible comparing with Mg. Thus, the amorphous phase and solid solution containing Mg created in sintering induce the most evaporation behavior of material for lunar regolith simulant CLRS-1 in vacuum sintering, which is quite different from that in air. Thus, the fast evaporation of those substances in sintering process induced the formation of macro pores inside the sample. The major influence of different components and pore-forming mechanism for vacuum sintering of lunar regolith simulant CLRS-1 is clarified.

4. Conclusion

This study investigated the effect of vacuum on the sintering behavior of CLRS-1 lunar simulant. Porous samples with density of 1.19 g cm^{-3} can be obtained by sintering at 1100 °C under vacuum. The porous samples have quite low thermal conductivity at both daytime temperature on the Moon and under room temperature, are 0.265 W m^{-1} K^{-1} and 0.359 W m^{-1} K^{-1} respectively. Furthermore, the component evolution during sintering was summarized and mechanism of pore-forming was illustrated, namely the fast evaporation of low melting point solid solutions containing Mg led to the formation of macro pores inside the sample. These findings reveal important sintering properties and mechanism information for application of the lunar base construction material.

Acknowledgments

This work was grateful to financial support from the National Natural Science Foundation of China, China (No. 51302309), the Strategic Pioneer Program on Space Science, Chinese Academy of Sciences, China (Grant no. XDA15013700) and the Key Research Program of Chinese Academy of Sciences, China (Grant no. ZDRW-KT-2016-1). We are also grateful to Professor Yanping Lu and Guiwen Wang of Chongqing University and Dengmin Wang of University of Science and Technology of China for providing assistance with the testing of the samples.

Appendix A. Supporting information

Supplementary data associated with this article can be found in the online version at doi:10.1016/j.ceramint.2018.11.023

References

[1] N. Lovegren, Chemistry on the Moon: The Quest for Helium-3, 21st Century Science and Technology, 2014, pp. 1–14.
[2] M.B. Duke, B. Brad R, J. Diaz, Lunar resource utilization: implications for commerce and exploration, Adv. Space Res. 31 (2003) 2413–2419, https://doi.org/10.1016/

S0273-1177(03)00550-7.
[3] H. Kawamoto, K. Shirai, Electrostatic transport of lunar soil for in situ resource utilization, J. Aerosp. Eng. 25 (2012) 132–138, https://doi.org/10.1061/(asce)as.1943-5525.0000094.
[4] P. Gordon, A. Colozza, A. Hepp, R. Heller, R. Gustafson, T. Stern, T. Nakamura, Thermal energy process heat for lunar ISRU: technical challenges and technology opportunities, in: Proceedings of the 49th AIAA Aerospace Sciences Meeting Including the New Horizons Forum and Aerospace Exposition, 2011. ⟨http://dx.doi.org/10.2514/6.2011-704⟩.
[5] L.A. Taylor, C.M. Pieters, D. Britt, Evaluations of lunar regolith simulants, Planet. Space Sci. 126 (2016) 1–7, https://doi.org/10.1016/j.pss.2016.04.005.
[6] P.E. Hintze, S. Quintana, Building a lunar or martian launch pad with In Situ materials: recent laboratory and field studies, J. Aerosp. Eng. 26 (2013) 134–142, https://doi.org/10.1061/(asce)as.1943-5525.0000205.
[7] G. Cesaretti, E. Dini, X. De Kestelier, V. Colla, L. Pambaguian, Building components for an outpost on the Lunar soil by means of a novel 3D printing technology, Acta Astronaut. 93 (2014) 430–450, https://doi.org/10.1016/j.actaastro.2013.07.034.
[8] T. Gualtieri, A. Bandyopadhyayn, Compressive deformation of porous lunar regolith, Mater. Lett. 143 (2015) 276–278, https://doi.org/10.1016/j.matlet.2014.11.153.
[9] L.A. Taylor, Microwave sintering of lunar soil: properties, theory, and practice, J. Aerosp. Eng. 18 (2005) 188–196, https://doi.org/10.1061//asce/0893-1321/2005/18:3/188.
[10] L.A. Taylor, T.T. Meek, Microwave processing of lunar soil, Adv. Astronaut. Sci. 108 (2004) 109–123.
[11] X. Gong, D.A. Paige, M.A. Siegle, Y.-Q. Jin, Inversion of dielectric properties of the lunar regolith media with temperature profiles using Chang'e microwave radiometer observations, IEEE Geosci. Remote Sensing 12 (2015) 384–388, https://doi.org/10.1109/LGRS.2014.2343617.
[12] A. Goulas, R.J. Friel, 3D printing with moondust, Rapid Prototyp. J. 22 (2016) 864–870, https://doi.org/10.1108/rpj-02-2015-0022.
[13] N. Labonnote, A. Rønnquist, B. Manum, P. Rüther, Additive construction: state-of-the-art, challenges and opportunities, Autom. Constr. 72 (2016) 347–366, https://doi.org/10.1016/j.autcon.2016.08.026.
[14] A. Goulas, J.G.P. Binner, R.A. Harris, R.J. Friel, Assessing extraterrestrial regolith material simulants for in-situ resource utilisation based 3D printing, Appl. Mater. Today 6 (2017) 54–61, https://doi.org/10.1016/j.apmt.2016.11.004.
[15] V.K. Balla, L.B. Roberson, G.W. O'Connor, S. Trigwele, S. Bose', A. Bandyopadhyay, First demonstration on direct laser fabrication of lunar regolith parts, Rapid Prototyp. J. 18 (2011) 451–457, https://doi.org/10.1108/13552541211271992.
[16] R.P. Mueller, L. Sibille, P.E. Hintze, T.C. Lippitt, J.G. Mantovani, M.W. Nugent, I.I. Townsend, Additive construction using basalt regolith fines, Eng. Sci. Constr. Oper. Challenging Environ. Earth Sp. (2015), https://doi.org/10.1061/9780784479179.042.
[17] M. Fateri, A. Gebhardt, Process parameters development of selective laser melting of lunar regolith for on-site manufacturing applications, Int. J. Appl. Ceram. Technol. 12 (2015) 46–52, https://doi.org/10.1111/ijac.12326.
[18] R. Winston, T. Nakamura, J.M. Gordon, B.K. Smith, Solar thermal system for lunar ISRU applications: development and field operation at Mauna Kea, HI, in: AIAA 49th Aerospace Science Meeting, 8124, 2011, pp. 1889-1896. ⟨http://dx.doi.org/10.1117/12.892810⟩.
[19] A. Meurisse, A. Makaya, C. Willsch, M. Sperl, Solar 3D printing of lunar regolith, Acta Astronaut. (2018), https://doi.org/10.1016/j.actaastro.2018.06.063.
[20] D.F. Heaney, Vacuum Sintering, in Sintering of Advanced Materials, Woodhead Publishing Limited, Cambridge, U.K, 2010.
[21] L. Jin, G. Zhou, S. Shimai, J. Zhang, S. Wang, ZrO_2-doped Y_2O_3 transparent ceramics via slip casting and vacuum sintering, J. Eur. Ceram. Soc. 30 (2010) 2139–2143, https://doi.org/10.1016/j.jeurceramsoc.2010.04.004.
[22] G. Mata-Osoro, J.S. Moya, C. Pecharroman, Transparent alumina by vacuum sintering, J. Eur. Ceram. Soc. 32 (2012) 2925–2933, https://doi.org/10.1016/j.jeurceramsoc.2012.02.039.
[23] D. Huo, Y. Zheng, X. Sun, X. Li, S. Liu, Preparation of transparent Y_2O_3 ceramic by slip casting and vacuum sintering, J. Rare Earth 30 (2012) 57–62, https://doi.org/10.1016/s1002-0721(10)60639-4.
[24] A. Meurisse, J.C. Beltzung, M. Kolbe, A. Cowley, M. Sperl, Influence of mineral composition on sintering lunar regolith (04017014-1-04017014-8), J. Aerosp. Eng. 30 (2017), https://doi.org/10.1061/(asce)as.1943-5525.0000721.
[25] Y. Zheng, S. Wang, Z. Ouyang, Y. Zou, J. Liu, C. Li, X. Li, J. Feng, CAS-1 lunar soil simulant, Adv. Space Res. 43 (2009) 448–454, https://doi.org/10.1016/j.asr.2008.07.006.
[26] C. Wang, L. Zeng, W. Yu, L. Zhang, Y. Guo, C. Gong, An electron beam linear scanning mode for industrial limited-angle nano-computed tomography, Rev. Sci. Instrum. 89 (2018) 015113, https://doi.org/10.1063/1.4993933.
[27] J. Kenneth, W. Street, C. Ray, D. Rickman, D.A. Scheiman, Thermal properties of lunar regolith simulants, Eng. Sci. Constr. Oper. Challenging Environ. 12th Earth Sp. (2010) 266–275, https://doi.org/10.1061/41096(366)28.
[28] M. Hillert, On the theory of normal and abnormal grain growth, Acta Metall. 13 (1965) 227–238, https://doi.org/10.1016/0001-6160(65)90200-2.
[29] S. Guo, Powder Sintering Theory, Metallurgical industry press, Beijing, China, 1998.
[30] G.-H. Hwang, H.-J. Jeon, Y.-S. Kim, Physical properties of barrier ribs of rlasma display panels: II, effects of fillers, J. Am. Ceram. Soc. 85 (2004) 2961–2964, https://doi.org/10.1111/j.1151-2916.2002.tb00563.x.
[31] A.J. Allen, S. Krueger, G. Skandan, G.G. Long, H. Hahn, H.M. Kerch, J.C. Parker, M.N. Ali, Microstructural evolution during the sintering of nanostructured ceramics oxides, J. Am. Ceram. Soc. 79 (1996) 1201–1212, https://doi.org/10.1111/j.1151-2916.1996.tb08573.x.
[32] E.J. Faierson, K.V. Logan, B.K. Stewart, M.P. Hunt, Demonstration of concept for fabrication of lunar physical assets utilizing lunar regolith simulant and a geothermite reaction, Acta Astronaut. 67 (2010) 38–45, https://doi.org/10.1016/j.actaastro.2009.12.006.
[33] F. Batool, M.M. Rafi, V. Bindiganavile, Microstructure and thermal conductivity of cement-based foam: a review, J. Build. Eng. 20 (2018) 696–704, https://doi.org/10.1016/j.jobe.2018.09.008.
[34] H. Uysal, R. Demirboğa, R. Şahin, R. Gül, The effects of different cement dosages, slumps, and pumice aggregate ratios on the thermal conductivity and density of concrete, Cem. Concr. Res. 34 (2004) 845–848, https://doi.org/10.1016/j.cemconres.2003.09.018.
[35] A.S. Pinheiro, Z.M. da Costa, M.J.V. Bell, V. Anjos, S.T. Reis, C.S. Ray, Thermal characterization of glasses prepared from simulated compositions of lunar soil JSC-1A, J. Non-Cryst. Solids 359 (2013) 56–59, https://doi.org/10.1016/j.jnoncrysol.2012.09.027.
[36] S. Yang, W. Tao, Heat Transfer, fourth ed., Higher Education Press, Beijing, China, 2006.
[37] L. Verdolotti, E. Di Maio, M. Lavorgna, S. Iannace, Hydration-induced reinforcement of rigid polyurethane–cement foams: mechanical and functional properties, J. Mater. Sci. 47 (2012) 6948–6957, https://doi.org/10.1007/s10853-012-6642-5.
[38] S.S. Schreiner, J.A. Dominguez, L. Sibille, J.A. Hoffman, Thermophysical property models for lunar regolith, Adv. Space Res. 57 (2016) 1209–1222, https://doi.org/10.1016/j.asr.2015.12.035.
[39] B.L. Cooper, Sintering of Lunar and Simulant Glass, Space Technology and Applications International Forum-STAIF, 969, 2008, pp. 186–194. ⟨http://dx.doi.org/10.1063/1.2844966⟩.
[40] C.H. Simonds, Sintering and hot pressing of Fra Mauro composition glass and the lithification of lunar breccias, Am. J. Sci. 273 (1973) 428–439, https://doi.org/10.2475/ajs.273.5.428.
[41] W. Kingery, H. Bowen, D. Uhlmann, Introduction to Ceramics, 2nd edition, John Wiley & Sons, New York, USA, 1979.
[42] J.T. Kohli, J.E. Shelby, Formation and properties of rare-earth aluminosilicate glasses, Phys. Chem. Glass. 32 (1991) 67–71.
[43] X. Li, Aluminosilicate glass, Glass Technol. 4 (1991) 45–54.
[44] Z. Chen, Chemical Thermodynamics of Refractories, Metallurgical industry press, Beijing, 2005.
[45] W. Dong, H. Jain, M.P. Harmer, Liquid phase sintering of alumina, III. Effect of trapped gases in pores on densification, J. Am. Ceram. Soc. 88 (2005) 1714–1719, https://doi.org/10.1111/j.1551-2916.2005.00149.x.
[46] L. Barbieri, F. Bondioli, I. Lancellotti, C. Leonelli, M. Montorsi, A.M. Ferrari, P. Miselli, The anorthite-diopside system: structural and devitrification study. Part II: crystallinity analysis by the Rietveld-RIR method, J. Am. Ceram. Soc. 88 (2005) 3131–3136, https://doi.org/10.1111/j.1551-2916.2005.00578.x.
[47] P. Alizadeh, V.K. Marghussian, The effect of compositional changes on the crystallization behaviour and mechanical properties of diopside-wollastonite glass-ceramics in the $SiO_2 \pm CaO \pm MgO$ (Na_2O) system, J. Eur. Ceram. Soc. 20 (2000) 765–773.
[48] J.J. Papike, M. Cameron, Crystal chemistry of silicate minerals of geophysical interest, Rev. Geophys. Space Phys. 14 (1976) 37–80, https://doi.org/10.1029/RG014i001p00037.
[49] C. Yong, Y. Lei, L. Tao, Y. Jingkun, Study on the reaction kinetics of forsterite synthesis, J. Northeast Univ.: Nat. Sci. 34 (2013) 111–113.